Thin-Walled Structures 182 (2023) 110214

Contents lists available at ScienceDirect

Thin-Walled Structures

journal homepage: www.elsevier.com/locate/tws

Full length article

Effects of contact friction and ply blocking on the crush behaviour of thin-walled composite structures: A numerical study

Haibao Liu [a,*], Jin Zhou [b], Di Zhang [b], Shipeng Li [c], Ioannis Giannopoulos [a]

[a] Centre for Aeronautics, School of Aerospace, Transport and Manufacturing, Cranfield University, Cranfield MK43 0AL, UK
[b] School of Mechanical Engineering, Xi'an Jiaotong University, Xi'an, Shaanxi 710049, China
[c] Key Laboratory of Mechanism Theory and Equipment Design of Ministry of Education, Tianjin University, Tianjin 300350, China

ARTICLE INFO

Keywords:
Thin-walled composite structures
Crashworthiness
Computational mechanics
Energy absorption
Damage mechanisms

ABSTRACT

The present paper presents a three-dimensional composite damage model for predicting the crush response of thin-walled structures, i.e., cylindrical tubes, manufactured employing fibre-reinforced polymer–matrix composites. This computational model is based upon a Continuum Damage Mechanics (CDM) approach and accounts for both the intralaminar and interlaminar damage as well as nonlinear behaviour that occur in the composite materials. Experimental data, obtained from published literature, are employed to validate the proposed composite damage model. A comparison between the experimental and computationally predicted results, including the load response, energy absorption and damage morphology, shows good agreement. Subsequently, the validated computational model is employed to investigate the effects of contact friction and ply blocking on the crush response of thin-walled composite structures. The results reveal that the friction between the tube/platen surfaces has a positive effect on the crushing performance of the composite structures and the ply blocking can somehow inhibit the crushing performance of the investigated composite structures.

1. Introduction

To save weight and achieve subsequent lower emissions, composite materials, based upon a polymeric-matrix and continuous carbon fibres, have been increasingly used in the aeronautical and automotive sectors [1–3]. As a key part of the safety and performance assessments, the crashworthiness of the composite structure needs to be determined. However, the experimental testing of manufactured composite structures is costly and time consuming [4]. For this reason, lower cost and more efficient evaluation methods are required for the crashworthiness assessments of composite structures. This has driven the development of computational, numerical models, which can accurately predict the crush behaviour of such composite structures.

The complex damage mechanisms of composite structures under crush loading brings considerable challenges to the development of high-fidelity computational models and a number of commercial packages have provided finite element-based models for assessing the crushing performances of composite structures. Typical examples include numerical models offered by LS-DYNA [5], PAM-CRASH [6], and ABAQUS [7]. These models have been used and developed in several papers [8–10]. Some examples are Xiao et al. [11] employed the composite material model 'MAT058' from LS-DYNA to simulate the axial crush tests on braided composite tubes. The comparison between the experimental and computational results revealed that the predicted peak load generally agreed well with the experimental value, whilst the steady-state predicted load was lower than the experimental value, with corresponding differences in the extent of energy absorption during the crash tests. The authors claimed that this under-prediction of the energy absorption was caused by the inability to model the elastic–plastic material response in the LS-DYNA 'MAT058' model. Johnson and David [12] conducted a quasi-static crush simulation of composite tubes using the meso-scale ply damage model implemented in PAM-CRASH. Extensive test programmes were conducted to obtain the material parameters for the modelling studies. The calibrated model was then used to predict the crushing load and energy absorption of the composite tube. Dali et al. [13] used the ABAQUS built-in orthotropic composite damage model combined with the ABAQUS 'C-Zone' add-on model to predict the behaviour of the crash-front of a Formula One racing car. Parameters required for the computational model were obtained from a series of physical calibration tests. The comparison between the experimental and modelling results showed that their modelling studies could deliver reasonable quantitative predictions at a reasonable computational cost. However, these researchers also reported that the progressive deviation observed from the experimental load versus displacement traces was not observed in the simulation results. This indicates that the complex interacting failure modes during

* Corresponding author.
E-mail address: haibao.liu@cranfield.ac.uk (H. Liu).

https://doi.org/10.1016/j.tws.2022.110214
Received 18 July 2022; Received in revised form 2 September 2022; Accepted 30 September 2022
Available online xxxx
0263-8231/© 2022 The Author(s). Published by Elsevier Ltd. This is an open access article under the CC BY license (http://creativecommons.org/licenses/by/4.0/).

damage evolution may not be captured by the CZone add-on model in ABAQUS and further investigation is needed.

As mentioned above, to achieve a better predictive capability, these commercial models generally require a large number of physical tests on representative test coupons to provide the calibration data, which can consume considerable time and effort. In addition, these commercially available models are generally based on shell elements, in which the through-thickness stresses were neglected, and a Two-Dimensional (2D) plane stress state was adopted. It is generally considered that neglecting through-thickness stress is not appropriate for composite structures under crush loading, due to the complex stress interaction and damage mechanisms in such structures. As a result, more advanced damage models, which require less physical testing and accommodate a three-dimensional stress state, are needed to predict accurately the crush behaviour of composite structures [14,15]. Israr et al. [16] developed a progressive damage model, based on the physical observations, to predict the behaviour of composite plates subjected to low velocity crushing. Two different damage criteria were implemented in their model, one is a localised crushing criterion and the other is the inside ply damage criterion. The former was applied to the elements at the crash-front of the composite structures, which have free faces and exhibit elastic–plastic behaviour during crush, and the latter was used in the elements behind the crash-front, which usually exhibit an elastic behaviour during crush. Israr et al. [16] showed that the proposed computational methodology is able to predict the force and displacement, as well as the main failure mechanisms and the overall deformation processes observed during the crush experiments. Tan and Falzon [17,18] developed a finite element-based damage model, which integrated a semi-empirical nonlinear shear model, to capture the crush response of the self-supporting corrugated-shaped composite structures. The force versus displacement curves, damage morphology and energy dissipation, obtained from the numerical simulation, were compared with the experimental results and showed a good agreement. Their study also further confirmed that the nonlinearity is of great importance for accurately modelling the crush behaviour of composites.

In the present paper, a Three-Dimensional (3-D) progressive damage model [19–21], which is based on the actual physical damage mechanisms and the interaction of the failure mechanisms, is developed to capture the crush behaviour of composite structures. This model will also take into account the nonlinear response of the composite materials. Compared to the commercially available predictive tools, this damage model only requires the intrinsic materials properties as the input parameters and does not require any model calibration steps. To confirm the capability and versatility of this three-dimensional composite damage model, it is employed to predict the crush behaviour of thin-walled composite structures, i.e., composite cylindrical tubes, which are especially designed to absorb energy upon being subjected to a compressive load. The predicted results from this numerical model, including the loading response, energy absorption and damage morphology, are compared with the experimental results previously reported in [22]. The developed model was then also employed to investigate the effects of friction and ply blocking on the crushing performance of composite cylindrical tubes, by conducting a set of simulations with different composite layups and friction coefficients. The novelty of this work is to investigate the complex deformation and damage mechanisms of composites under crushing load, and reveal the influencing mechanisms of contact friction and ply blocking on the crush performance of thin-walled composite structures. It is expected that the present elastic–plastic damage model along with the relevant study method and results can provide guidance to the design of crashworthy thin-walled composite structures.

2. Theoretical

2.1. The intralaminar damage model

Damage initiation. The material response of unidirectional ply in fibre-dominated direction is assumed to be elastic. Strain-based failure criteria were defined to capture the initial damage of unidirectional ply in fibre-dominated direction and given by,

$$F_{fib}^{T}\left(\varepsilon_{fib}\right)=\left(\frac{\varepsilon_{fib}}{\varepsilon_{fib}^{OT}}\right)^{2}\geq 1, \tag{1}$$

$$F_{fib}^{C}\left(\varepsilon_{fib}\right)=\left(\frac{\varepsilon_{fib}}{\varepsilon_{fib}^{OC}}\right)^{2}\geq 1, \tag{2}$$

where F_{fib}^{T} and F_{fib}^{C} are the failure indices for tension and compression, respectively. The strains at fibre tensile and compressive damage initiation are represented by ε_{fib}^{OT} and ε_{fib}^{OC}, respectively. In this criterion, ε_{fib} is the current strain along the fibre-dominated direction which is corresponded to the longitudinal direction in the unidirectional ply.

The initiation failure criteria developed according to the theories proposed by Puck and Schürmann [23] and Catalanotti [24] et al. was used to capture the transverse (matrix-dominated) and through-thickness (matrix-dominated) initiation damage in unidirectional ply. The strain-based damage initiation function was used to define the thorough-thickness initiation damage in woven ply. The matrix-dominated failure criteria are given below,

$$F_{mat}=\left(\frac{\sigma_{NN}}{S_{23}^{A}}\right)^{2}+\left(\frac{\sigma_{NT}}{S_{23}^{A}}\right)^{2}+\left(\frac{\sigma_{LN}}{S_{12}^{A}}\right)^{2}+\lambda\left(\frac{\sigma_{NN}}{S_{23}^{A}}\right)\left(\frac{\sigma_{LN}}{S_{12}^{A}}\right)^{2}+\kappa\left(\frac{\sigma_{NN}}{S_{23}^{A}}\right) for\ \sigma_{NN}>0, \tag{3}$$

$$F_{mat}=\left(\frac{\sigma_{NT}}{S_{23}^{A}-\mu_{NT}\sigma_{NN}}\right)^{2}+\left(\frac{\sigma_{LN}}{S_{12}^{A}-\mu_{LN}\sigma_{NN}}\right)^{2} for\ \sigma_{NN}\leq 0, \tag{4}$$

where F_{mat} is the failure index for matrix tensile and compressive failure. In Eqs. (11) and (12), $\sigma_{ij}(i,j=N,T,L)$ are the stresses on the fracture surface of unidirectional lamina. Parameters λ and κ are defined by $\lambda=2\mu_{LN}S_{23}^{A}/S_{12}^{A}-\kappa$, and $\kappa=(S_{12}^{A\,2}-\left(Y_{T}\right)^{2})/S_{23}^{A}Y_{T}$, where S_{12}^{A} and S_{23}^{A} are the shear strengths. The transverse friction coefficients, μ_{NT} and μ_{LN}, are defined based on Mohr–Coulomb theory where $\mu_{NT}=-1/tan\left(2\theta_{f}\right)$, $S_{23}^{A}=Y_{C}/2tan\left(\theta_{f}\right)$ and $\mu_{LN}=\mu_{NT}S_{12}^{A}/S_{23}^{A}$, Y_{T} and Y_{C} are the transverse tensile strength and transverse compressive strength, respectively. θ_{f} is the rotation angle described in [25].

Damage evolution. Several monotonically increasing damage variables ranging from 0 (no damage) to 1 (complete failure) were defined to indicate the damage degree of composite laminates under different loading cases. d_{fib}^{T} and d_{fib}^{C} are related to the fibre-dominated tensile and compressive damage, respectively. d_{mat} indicates the evolution of matrix damage due to a combination of transverse tension/compression and shear loading.

$$d_{fib}^{T(C)}=\frac{\varepsilon_{fib}^{FT(C)}}{\varepsilon_{fib}^{FT(C)}-\varepsilon_{fib}^{OT(C)}}\left(1-\frac{\varepsilon_{fib}^{OT(C)}}{\varepsilon_{fib}^{T(C)}}\right), \tag{5}$$

$$d_{mat}=\frac{\varepsilon_{r}^{f}-\varepsilon_{r,in}^{0}}{\varepsilon_{r}^{f}-\varepsilon_{r}^{0}}\left(1-\frac{\varepsilon_{r}^{0}-\varepsilon_{r}}{\varepsilon_{r}-\varepsilon_{r,in}^{0}}\right). \tag{6}$$

In Eq. (5) the initiation strains, $\varepsilon_{fib}^{OT(C)}$, at which the damage initiation occurs, are determined by the material strength $X_{fib}^{T(C)}$. $\varepsilon_{fib}^{FT(C)}$ is the failure strain for unidirectional ply. In Eq. (6), ε_{r}^{0} and $\varepsilon_{r,in}^{0}$ are the l^{2}-norm of overall strain and elastic strain at damage initiation, respectively. ε_{r}^{f} is the l^{2}-norm of failure strain and ε_{r} is the l^{2}-norm of current strains acting on the fracture plane. The final failure strain, $\varepsilon_{ij}^{f}(i,j=1,2,3)$, can be determined by:

$$\varepsilon_{ij}^{f}=2G_{c}|_{ij}/(\sigma_{ij}^{0}l_{c}) \tag{7}$$

where the respective values of $G_{c}|_{ij}$ are the tensile, $G_{Ic}|_{ft}$, and compressive, $G_{Ic}|_{fc}$, intralaminar ply fracture energies in the longitudinal fibre-direction and the tensile, $G_{Ic}|_{mt}$, compressive, $G_{Ic}|_{mc}$, and shear, $G_{IIc}|_{ms}$, intralaminar ply fracture energies in the transverse directions.

The term σ_{ij}^0 is the stress corresponding to damage initiation and l_c is the characteristic length which can be determined based on the volume of the elements.

2.2. The interlaminar damage model

The built-in surface-based cohesive behaviour in ABAQUS/Explicit was used to capture the delamination in composite structures using a bilinear traction-separation relationship. The interlaminar failure initiation is governed by a quadratic stress criterion,

$$\left(\frac{\langle t_{33}\rangle}{t_{33}^0}\right)^2+\left(\frac{t_{31}}{t_{31}^0}\right)^2+\left(\frac{t_{32}}{t_{32}^0}\right)^2=1 \tag{8}$$

where the term $t_i(i = 33, 31, 32)$ represents the current normal or shear stresses and $t_i^0\,(i = 33, 31, 32)$ represents the normal and shear cohesive strengths. The corresponding displacements are denoted by δ_{33}, δ_{31} and δ_{32}, and by δ_{33}^0, δ_{31}^0 and δ_{32}^0, respectively. The energy-based Benzeggagh–Kenane (B–K) criterion for Mixed-mode propagation was used to derive a total value G_c for the growth of the delamination between the composite plies and is given by:

$$G_c = G_{Ic} + (G_{IIc} - G_{Ic})\left(\frac{G_{II}}{G_I + G_{II}}\right)^{\eta} \tag{9}$$

where G_{Ic} is the Mode I (opening tensile), G_{IIc} is the Mode II (in-plane shear) interlaminar fracture energy. The values of G_{Ic}, G_{IIc} and η may all be experimentally measured and so inputted into the FEA model. The parameters G_I and G_{II} are the current Mode I and Mode II energy-release rates, respectively, as calculated from the FEA code. The parameter η is the B–K Mixed-mode interaction exponent, which can be determined based on ASTM D6671/D6671M-03 [26] testing standard.

2.3. Nonlinear behaviour model

In this research, An extended elastic–plastic model has been used to capture the nonlinear material response prior to the damage initiation, since this enables a more accurate prediction of the crush behaviour of the composite laminate. The global coordinate system is defined as X–Y–Z and the material coordinate system is defined as 1–2–3.

The effective stress, σ_{eff}. For a general 3-D fibre-reinforced composite, a quadratic stress-based yield function, arising from the results of a micromechanical FEA approach, was proposed [27,28]:

$$\begin{aligned}2f\left(\sigma_{ii}\right) = {} & a_{11}\sigma_{11}^2 + a_{22}\sigma_{22}^2 + a_{33}\sigma_{33}^2 + 2a_{12}\sigma_{11}\sigma_{22} \\ & + 2a_{13}\sigma_{11}\sigma_{33} + 2a_{23}\sigma_{22}\sigma_{33} \\ & + 2a_{44}\tau_{23}^2 + 2a_{55}\tau_{13}^2 + 2a_{66}\tau_{12}^2\end{aligned} \tag{10}$$

where f is the plastic potential. The coefficients, $a_{ij}(i, j = 1, 2, 3, 4, 5, 6)$, which describe the extent of anisotropy in the plastic behaviour of the composite, are assumed to be constant and may be determined experimentally.

To develop the elastic–plastic model for the intralaminar response of composite materials under a complex stress state, Sun and Chen [27,29,30] defined an effective stress and an effective plastic strain for modelling the plastic constitutive relationship between the stress and strain. The 3-D effective stress, σ_{eff}, for a transversely isotropic composite that is linearly-elastic in the fibre direction, can be derived from the above quadratic stress-based yield function, and is given by [31]:

$$\sigma_{eff} = \sqrt{\frac{3}{2}\left(\sigma_{22}^2 + \sigma_{33}^2\right) - 3\sigma_{22}\sigma_{33} + 3a_{44}\sigma_{23}^2 + 3a_{55}\sigma_{13}^2 + 3a_{66}\sigma_{12}^2} \tag{11}$$

For transversely isotropic elastic solids, the value of the coefficient a_{44}, associated with the term σ_{23}^2, can be set as having a value of two, by assuming the equivalency between plastic potential and strain energy. In transversely isotropic materials, i.e. a unidirectional fibre reinforced composite, the coefficient a_{55}, associated with σ_{13}^2, is equal to the coefficient a_{66}, associated with σ_{12}^2. Now, the coefficient a_{66} can be readily determined from off-axis experiments conducted at different values of the off-axis angle using a unidirectional composite.

The effective plastic strain, ε_{eff}^p. The total strain can be linearly decomposed into the elastic strain and the plastic strain, assuming infinitesimal strain conditions. The normal strains are given by:

$$\varepsilon_{ii} = \varepsilon_{ii}^e + \varepsilon_{ii}^p \tag{12}$$

and the shear strains are given by:

$$\gamma_{ij} = \gamma_{ij}^e + \gamma_{ij}^p \tag{13}$$

An effective plastic strain, ε_{eff}^p, which gives a measure of the amount of plasticity in the composites, was given by:

$$\varepsilon_{eff}^p = \frac{\varepsilon_{XX}^p}{H(\theta)} \tag{14}$$

where the term $H(\theta)$ is given by:

$$H(\theta) = \sqrt{\frac{3}{2}sin^4\theta + 3a_{66}sin^2\theta cos^2\theta} \tag{15}$$

The value of the single parameter, a_{66} can be readily determined experimentally from off-axis tests conducted at different values of the off-axis angle, θ. The term ε_{XX}^p is the plastic strain resulting from the uniaxially applied load in the X-direction and is given by:

$$\varepsilon_{XX}^p = \varepsilon_{XX} - \frac{\sigma_{XX}}{E_{XX}} \tag{16}$$

In the above equation, E_{XX}, is the elastic modulus in the loading direction which can be calculated from the material properties and off-axis angle employed in the test as given in [27]:

$$E_{XX} = \frac{1}{\frac{1}{E_{11}}\cos^4\theta + \frac{1}{E_{22}}\sin^4\theta + \left(\frac{1}{G_{12}} - \frac{2\nu_{12}}{E_{11}}\right)\sin^2\theta\cos^2\theta} \tag{17}$$

where E_{11} and E_{22} are the elastic moduli, ν_{12} is the Poisson's ratio and G_{12} is the elastic shear modulus. To characterise the relationship between the effective plastic strain, ε_{eff}^p, and the effective stress, σ_{eff}, a power law function can be used to fit all the effective stress versus effective plastic strain ($\sigma_{eff} - \varepsilon_{eff}^p$) data points from the off-axis angle experiments given by [27]:

$$\varepsilon_{eff}^p = A{\sigma_{eff}}^n. \tag{18}$$

where A and n are the nonlinear coefficients, which can give a best fit to the $\sigma_{eff} - \varepsilon_{eff}^p$ data points obtained from the different-angle off-axis tension experiments. The determination of the single parameter, a_{66}, and the nonlinear coefficients, A and n, facilitates the calculation of the elements in the incremental plastic strain tensor, $d\varepsilon_{ij}^p(i, j = 1, 2, 3)$, given by:

$$\begin{Bmatrix} d\varepsilon_{11}^p \\ d\varepsilon_{22}^p \\ d\varepsilon_{33}^p \\ d\varepsilon_{12}^p \\ d\varepsilon_{13}^p \\ d\varepsilon_{23}^p \end{Bmatrix} = \frac{An}{{\sigma_{eff}}^{1-n}} \begin{Bmatrix} 0 \\ 3(\sigma_{22} - \sigma_{33})/2\sigma_{eff} \\ 3(\sigma_{33} - \sigma_{22})/2\sigma_{eff} \\ 3a_{66}\tau_{12}/2\sigma_{eff} \\ 3a_{66}\tau_{13}/2\sigma_{eff} \\ 3a_{44}\tau_{23}/2\sigma_{eff} \end{Bmatrix} d\sigma_{eff} \tag{19}$$

The classic elastic constitutive equation for the stress versus strain relationship for orthotropic elasticity may be expressed as [32] Eq. (20) in Box I where $d\varepsilon_{ij}(i, j = 1, 2, 3)$ are the incremental total strain tensors and $d\sigma_{ij}(i, j = 1, 2, 3)$ are the incremental stress tensors. ν_{ij} are the Poisson's ratios and E_{ii} are the Young's moduli, either for tension or compression loading [7]. By combining the developed plastic model with the classic elastic model, the elastic–plastic constitutive relation for the response prior to damage initiation was obtained by Eq. (21) in Box II.

$$\begin{Bmatrix} d\varepsilon_{11} \\ d\varepsilon_{22} \\ d\varepsilon_{33} \\ d\varepsilon_{12} \\ d\varepsilon_{13} \\ d\varepsilon_{23} \end{Bmatrix} = \begin{bmatrix} 1/E_{11} & -\nu_{21}/E_{11} & -\nu_{31}/E_{11} & 0 & 0 & 0 \\ -\nu_{12}/E_{22} & 1/E_{22} & -\nu_{32}/E_{22} & 0 & 0 & 0 \\ -\nu_{13}/E_{33} & -\nu_{23}/E_{33} & 1/E_{33} & 0 & 0 & 0 \\ 0 & 0 & 0 & 1/G_{12} & 0 & 0 \\ 0 & 0 & 0 & 0 & 1/G_{13} & 0 \\ 0 & 0 & 0 & 0 & 0 & 1/G_{23} \end{bmatrix} \begin{Bmatrix} d\sigma_{11} \\ d\sigma_{22} \\ d\sigma_{33} \\ d\sigma_{12} \\ d\sigma_{13} \\ d\sigma_{23} \end{Bmatrix}, \tag{20}$$

Box I.

$$\begin{Bmatrix} d\varepsilon_{11} \\ d\varepsilon_{22} \\ d\varepsilon_{33} \\ d\varepsilon_{12} \\ d\varepsilon_{13} \\ d\varepsilon_{23} \end{Bmatrix} = \begin{bmatrix} 1/E_{11} & -\nu_{21}/E_{11} & -\nu_{31}/E_{11} & 0 & 0 & 0 \\ -\nu_{12}/E_{22} & 1/E_{22} & -\nu_{32}/E_{22} & 0 & 0 & 0 \\ -\nu_{13}/E_{33} & -\nu_{23}/E_{33} & 1/E_{33} & 0 & 0 & 0 \\ 0 & 0 & 0 & 1/G_{12} & 0 & 0 \\ 0 & 0 & 0 & 0 & 1/G_{13} & 0 \\ 0 & 0 & 0 & 0 & 0 & 1/G_{23} \end{bmatrix} \begin{Bmatrix} d\sigma_{11} \\ d\sigma_{22} \\ d\sigma_{33} \\ d\sigma_{12} \\ d\sigma_{13} \\ d\sigma_{23} \end{Bmatrix} + \begin{Bmatrix} d\varepsilon^{p}_{11} \\ d\varepsilon^{p}_{22} \\ d\varepsilon^{p}_{33} \\ d\varepsilon^{p}_{12} \\ d\varepsilon^{p}_{13} \\ d\varepsilon^{p}_{23} \end{Bmatrix}, \tag{21}$$

Box II.

2.4. Element deletion strategy

In the presented model, the element deletion strategy is based on the determinant of the deformation gradient, $Det\boldsymbol{F}$, which is an internal variable transferred to the VUMAT subroutine. $Det\boldsymbol{F}$ yields the ratio of the deformed volume, V, and undeformed, V_0 volume, of an element [32], given by:

$$Det\boldsymbol{F} = \frac{V}{V_0}, \tag{22}$$

The deformation gradient, $Det\boldsymbol{F}$, can provide a reasonable indication of element distortion. The overall element distortion criterion was subsequently based on both the fibre-dominated longitudinal damage parameter, d_{fib}, and limits on $Det\boldsymbol{F}$ for tracking large element deformation [33],

$$Delete\ element\ if \begin{cases} d_{fib} > 0.99 \\ Det\boldsymbol{F} < 0.6\ or\ Det\boldsymbol{F} > 1.8 \end{cases}. \tag{23}$$

The limits on $Det\boldsymbol{F}$ are user defined and the quoted values were found to yield reliable results. For more details of the present composite damage model, please refer to [20,33–37].

2.5. Model implementation

The overall flowchart for the three-dimensional finite element model for simulating the intralaminar and interlaminar impact damage is given in Fig. 1. The flowcharts for both the main model and the sub-level damage model, which was incorporated as a VUMAT into the main finite element model ('ABAQUS/Explicit 2018'), are presented. This numerical model has been described in detail elsewhere [19–21] and only the essential details are given below.

2.6. Mesh sensitivity study

In order to show the mesh independence of the proposed damage model, a mesh sensitivity study was carried out on simple 3D rectangular geometries under longitudinal compressive loading. Models with element sizes of 0.5 mm,1 mm, and 1.5 mm were created. The dimensions of the models were 10 mm × 4 mm × 1 mm and the out-of-plane displacement was constrained so that the rectangular specimens would not buckle under compressive loading. When the specimens fractured, the total longitudinal strain is approximately 0.7%. The loading responses of these three specimens are compared and shown in Fig. 2, confirming the mesh independence of the presented damage model.

3. Model validation methodology

3.1. Composite demonstrators

In this study, the tulip-triggered cylindrical composite tube with a layup of $[0/90]_{2S}$ reported in [22] were chosen as composite demonstrators to validate the developed computational model. As described in the literature, the loading rate of the experiments was set as 1 mm/s to make sure the crush event is quasi-static. The cylindrical tube are manufactured using the T700/2510 unidirectional carbon-epoxy prepregs. Experimental data including load response and damage morphology, proceeded from the tulip-triggered cylindrical composite tube, facilitate a good validation of the developed damage model. The geometry and dimensions of the composite cylindrical tube are shown in Fig. 3.

3.2. Finite element models

The FEA model for the simulation of crush tests on the tulip-triggered cylindrical tube is created in ABAQUS 2018 and shown in Fig. 4. For the part of the specimen which will be crushed by the rigid plate, the element size was defined as 1 mm in both the longitudinal and transverse directions [33,42,43], and the remain elements are defined as 5 mm in the longitudinal direction and 1 mm in the transverse direction. The C3D8R elements were selected, and three elements were assigned to the through-thickness direction of the composite ply in this study. The rotation and in-plane movement of rigid plate were restricted and only the vertical movement is allowable. The total numbers of the elements in the FEA model is 107 520. The general contact algorithm and surface-based cohesive behaviour were used to govern the global contact and composite interface contact, respectively [44]. An enhanced stiffness-based hourglass and distortion control were employed to suppress spurious energy modes. The friction coefficients of 0.2 and 0.25 were used for metal/composite and ply/ply interfaces, respectively [33,45]. The vertical loading speed applied in the model was fixed at 1000 mm/s, which can reduce computation time whilst ensuring that the no significant inertial effects on the simulation results. To achieve an acceptable simulation time, selective mass scaling was used to scale elements, which had a stable time increment below 1e-08 s, during the entire virtual crushing event [15]. Computations were completed using 32 CPUs on a Linux Cluster with a run time of 36 h. The material properties required for the simulation of the quasi-static crush on the tulip-triggered cylindrical tube are given in Table 1.

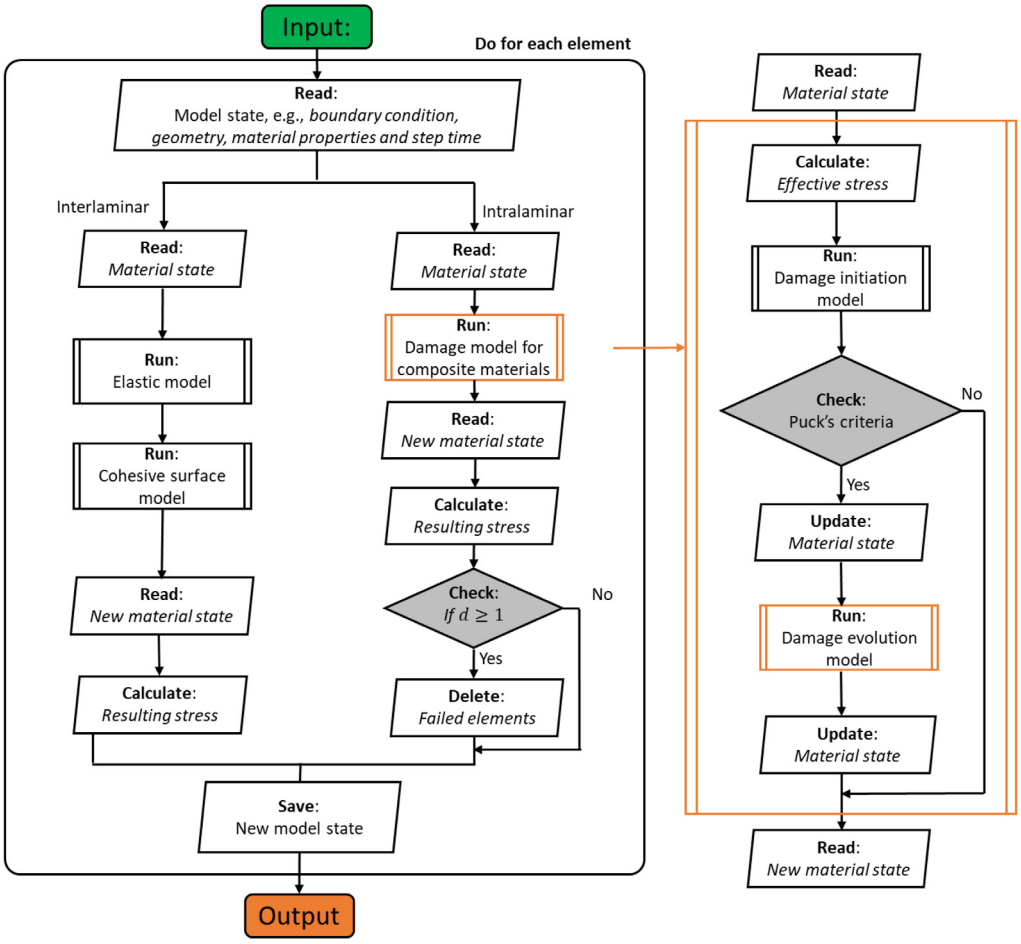

Fig. 1. The implementation of the FEA numerical model showing schematically the overall flowchart for one computational time-step and for a single element.

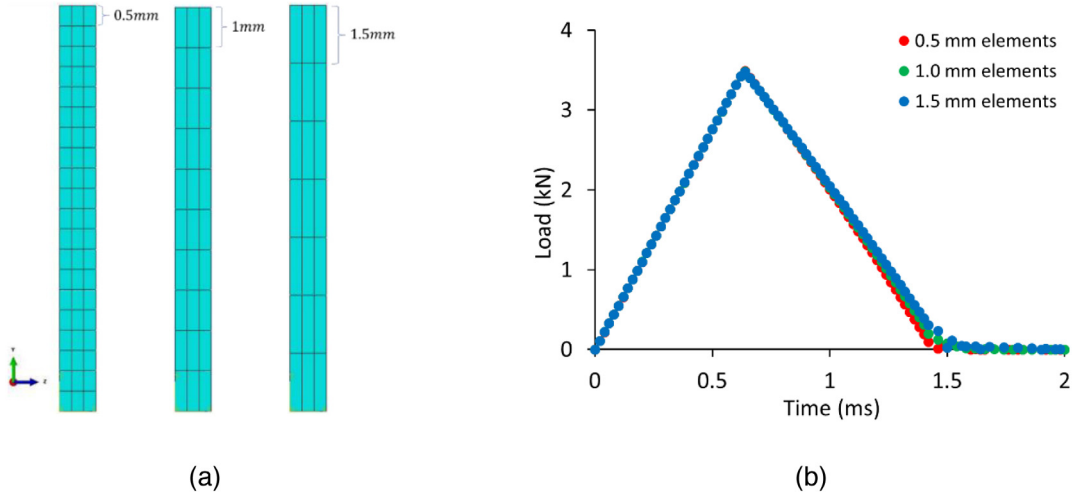

Fig. 2. Mesh sensitivity study set-up and results: (a) Specimens for mesh sensitivity studies and (b) corresponding load versus time histories obtained from virtual compression tests.

4. Comparison between experimental and computational results

4.1. Load response and energy absorption

The load versus displacement curves, energy absorption and crush efficiency obtained from the crushing experiment and simulation of tulip-triggered cylindrical tube are exhibited in Fig. 5. The loading response curves presented in Fig. 5a show that the cylindrical composite tube presented linear response prior to the peak point at the displacement of ca. 10 mm, which corresponded to the tulip trigger. After a peak load, a slight load drop was observed, which is followed by the steady-state response of the cylindrical composite tube. As for the experimental case, the predicted load response of the cylindrical tube also followed a linear response corresponding to the stage of trigger consumption and a steady-state response corresponding to the stage

Table 1
Properties of the composite plies in the tulip-triggered cylindrical tube [22,38–41].

Property	Tulip-triggered cylindrical tube
Moduli (GPa)	$E_{11} = 142; E_{22} = E_{33} = 8.4; G_{23} = 4.6; G_{12} = G_{13} = 4.6$
Poisson's ratio	$\nu_{23} = 0.32; \nu_{12} = \nu_{13} = 0.32$
Strength, S, values (MPa)	$S_{1t} = 2282; S_{2t} = S_{3t} = 65; S_{1c} = 1465; S_{2c} = S_{3c} = 290$ $S_{12} = S_{13} = S_{23} = 105$
Intralaminar ply fracture energies (kJ/m^2)	$G_{Ic}\|_{ft} = 108; G_{Ic}\|_{fc} = 58.4$
	$G_{Ic}\|_{mt} = 0.33; G_{Ic}\|_{mc} = 1.1; G_{IIc}\|_{ms} = 1.1$
Interlaminar fracture energies (kJ/m^2)	$G_{Ic} = 0.33; G_{IIc} = 1.1$
Benzeggagh–Kenane exponent	$\eta = 1.09$
Cohesive strengths (MPa)	$t^0_{33} = 60; t^0_{31} = t^0_{32} = 60$
Cohesive stiffness (MPa/mm)	$k_i = 5.6 \times 10^5$
Elastic–plastic coefficients, a_{66}, A and n	$a_{66} = 2.7;\ A = 3.14 \times 10^{-13}$ MPa^{-n}; $n = 4.19$

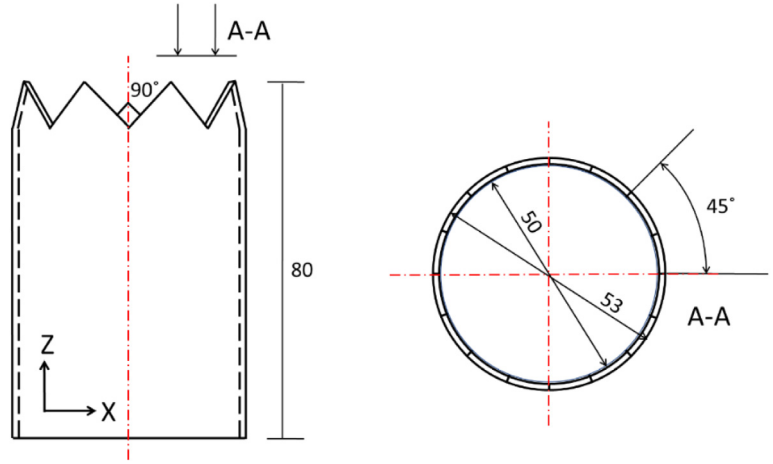

Fig. 3. Geometry and dimensions of the tulip-triggered cylindrical tube. All dimensions are in mm.

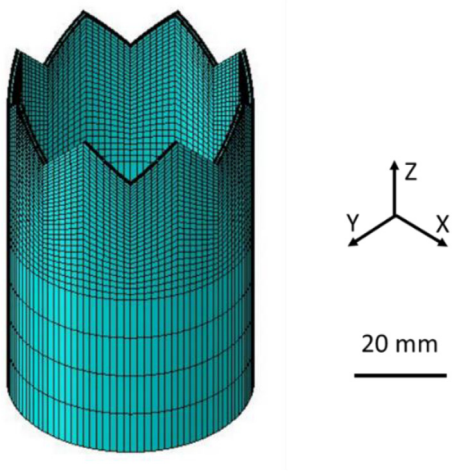

Fig. 4. Finite element models for the crush simulations of the tulip-triggered cylindrical tube.

of bulk tube consumption. The comparison between the experimental and numerical load versus displacement curves confirms that the developed composite model can accurately capture the load response of the composite cylindrical tube. In the experiments, the cylindrical tube delivered values of 433 J and 84% for energy absorption and crush efficiency respectively after 40 mm crushing displacement, as shown in Fig. 5b. The comparison, between the experimental and numerical values, showed a deviation less than 5%, which further confirmed the capability of the developed model in predicting the energy absorption behaviour of composite structures under crush loading.

In addition, to show the advantage of the elastic–plastic damage model, an elastic-only damage model was also employed in this study to predict the crushing response of the cylindrical composite tube. The loading responses and crushing energy proceed from the elastic-only and the elastic–plastic damage models are also compared in Figs. 5a and 5b. This comparison shows that the elastic-only damage model delivered slightly higher maximum load but lower steady-state load, compared to the elastic–plastic damage model. In terms of crushing energy, both the elastic-only and elastic–plastic models can yield a good agreement with experimental results, while the elastic-only damage model predicted a lower crushing efficiency (68%) compared to the elastic–plastic model, which delivered a crushing efficiency of 79%, showing a good agreement with the experimental crushing efficiency (84%).

4.2. Crush progression and damage morphology

Generally, when subjected to axial crush loading, composite laminates would present fibre fracture, fibre kinging, matrix cracking, delamination, ply splaying, fragmentation, debris and elastic bending. These failure modes have been schematically presented in a 0/90 cross-ply laminates as shown in Fig. 6, where v_0 represents the crushing velocity and all the fracture surfaces are highlighted in red lines.

The crush progression was extracted from the experiments and simulation for the tulip-triggered cylindrical tube and compared in Fig. 7, where d represents the displacement of the rigid plate. The eight tulip peaks provided trigger points for damage initiation, from where damage then propagates throughout the entire composite tube. The gradual consumption of the tulip triggers maximised the amount of damaged material and prevented any high peak load at the onset of crushing. When the crush transitioned to bulk tube, the outermost ply started to separate from the bulk tube and splits started to form in the outer 0° plies. At the steady-state bulk crush, these splits propagated along the direction parallel to the fibre direction and the ply bending formed to release the constraint on the inner plies, which

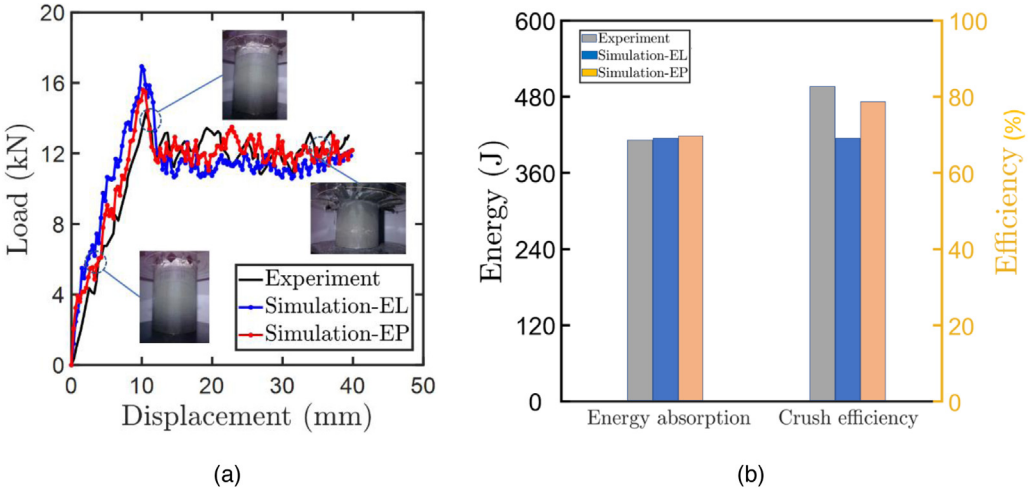

Fig. 5. Experimental and numerical load versus displacement curves, energy absorption and crush efficiency of the cylindrical tubes: (a) the load versus displacement curves, (b) the energy absorption and crush efficiency.
Source: Experimental data are obtained from [22], 'EL' refers to 'elastic-only' damage model and 'EP' refers to 'elastic–plastic' damage model.

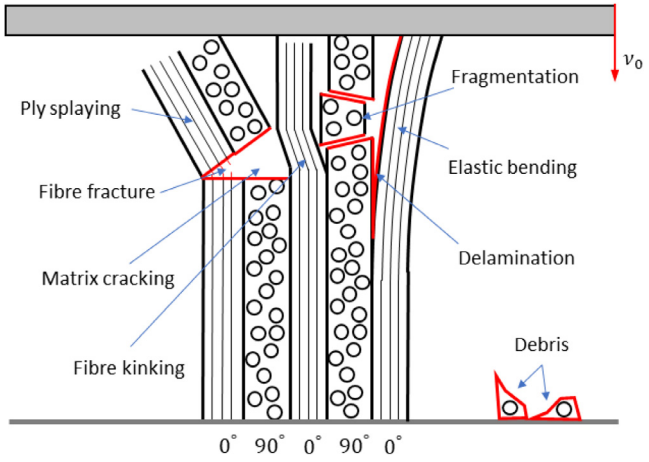

Fig. 6. Failure modes presented in composite laminates subjected to axial crush loading.

can reduce further intralaminar damage due to subsequent loading. The crush progression processes observed in the numerical simulation correlated very well with the two experimental cases, which confirmed the capability of the developed model in capturing the damage onset and propagation of composite structures under axial crush loading.

Fig. 8 shows the top views of the crushed composite tubes obtained from experiment and simulation. The experimental damage morphology shown in Fig. 8a presents that the outer plies splayed out and formed a funnel-like structure, in which the 0° plies tend to split into a number of wide bindles, and the 90° plies tend to form several wider segments. Due to confinement, the inner plies experienced substantial damage and generated a large number of segments, which were held in the hollow region of the tube. The inner 0° plies tended to break into smaller pieces and the inner 90° plies, similar with the outer 90° plies, also tended to break into several segments. Fig. 8b shows the numerically predicted damage morphology of the composite tube. It can be seen that the numerical model successfully predicted the morphology and different damage modes presented by the experimentally crushed composite tube.

To further confirm the capability of the model in capturing damage morphology, side views of the crushed composite cylindrical tubes obtained from experiment and simulation are also compared in Fig. 9. In the experimental side view shown in Fig. 9a, due to confinement, substantial intralaminar damage occurred in the region of crush front. In contrast, with less restriction, the outer plies tended to splay to the peripheral area, which eventually contributes to the formation of a delamination ahead of the intralaminar damage. The above sequence of damage was accurately reproduced by the developed composite model as shown in Fig. 9b. These comparisons between experimental and numerical damage morphology demonstrate well the capability of the developed composite model in predicting the deformation and damage of crushed composite structures.

5. Effects of the friction and blocking plies

5.1. Effects of the friction

It has been reported that the friction coefficient employed for the contact between the plate and composite specimen has unneglectable effects on the numerical results obtained from the crush simulation. In this work, the effects of friction coefficients were quantitatively studied by scaling the baseline value (0.2) to 0.1 and 0.4 in the employed simulation models. The total displacement is defined as 30 mm in this comparison study. The load versus displacement curves and energy absorption as well as crush efficiency obtained from simulations with different friction coefficients have been compared in Fig. 10. For comparison, the respective experimental results have also been exhibited. As shown in Fig. 10a, the model with friction coefficient of 0.4 delivered much higher load than the model with a baseline value, while the difference between the load responses obtained from the models with the baseline (0.2) and decreased (0.1) friction coefficient values seems not that significant. Through the comparison between these loads versus displacement traces, it can be found that the enhancing effects of the increasing friction coefficient were mainly observed at the loading increasing stage. Simulations with larger friction coefficients ($0.4 > 0.2 > 0.1$) tend to present larger peak load (23.1 kN > 15.2 kN > 14.8 kN). These enhancing effects still exist at the load steady state, but the gap between results obtained from simulations with different friction coefficients have become much smaller.

Fig. 10b shows the comparison of energy absorption and crush efficiency obtained from simulations with different friction coefficients. In terms of the energy absorption, the simulation with a friction coefficient of 0.4 presents the highest energy absorption (442.5 J), followed by the simulation with the baseline value (332.7 J) and then the simulation with a friction coefficient of 0.1 (298.1 J). In terms of the crush efficiency, the model with a friction coefficient of 0.4 showed a crush efficiency of 62.2%, which is much lower than the efficiencies

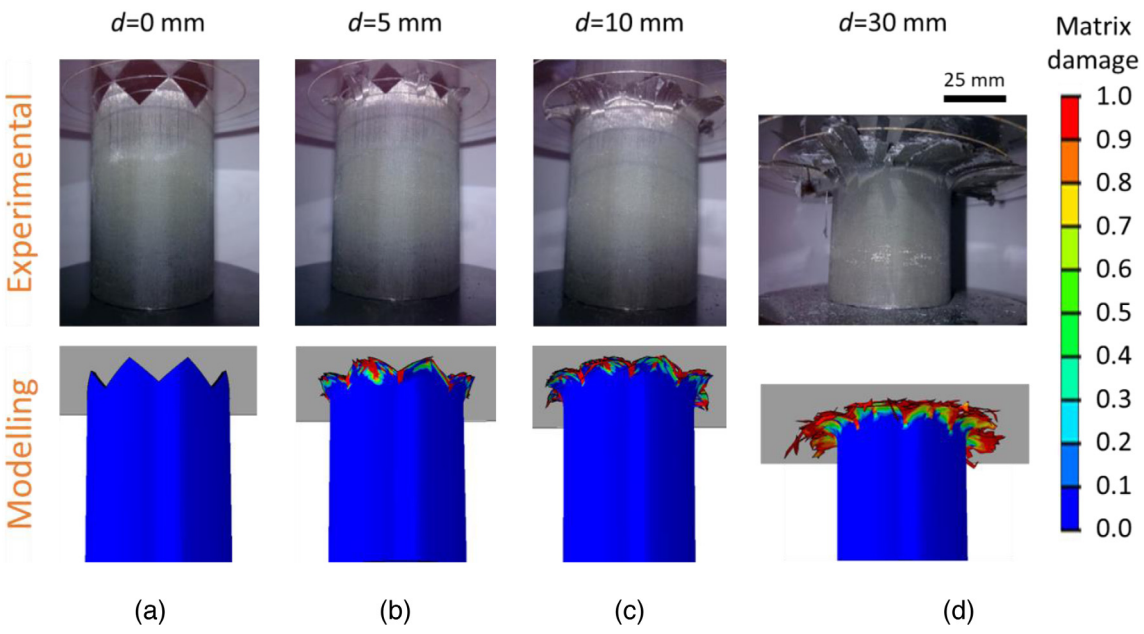

Fig. 7. Experimental and modelling crush progression of the cylindrical tubes: (a) initial state, (b) trigger consumption, (c) transition to bulk crushing and (d) steady-state bulk crushing.
Source: Experimental data are obtained from [22].

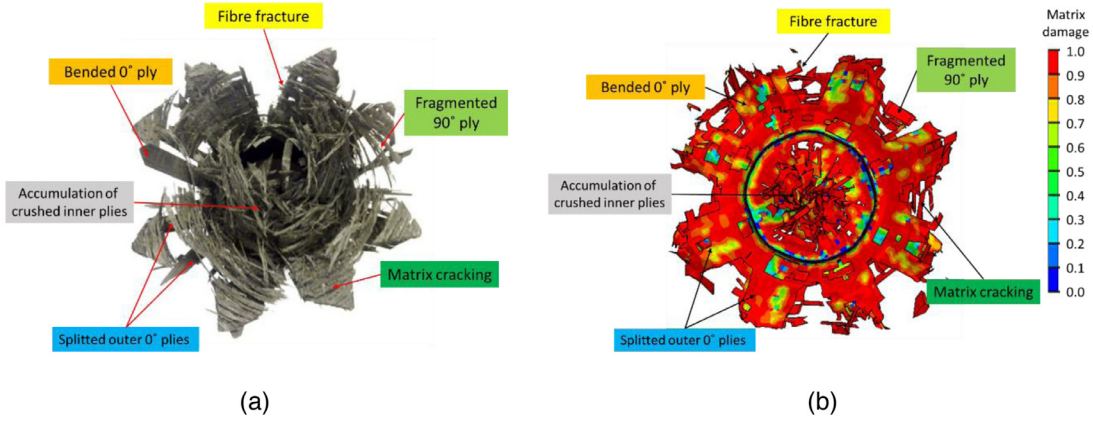

Fig. 8. Comparison of the top views of the crushed cylindrical tubes: (a) the experimentally observed damage morphology [22] and (b) the numerically predicted damage morphology.

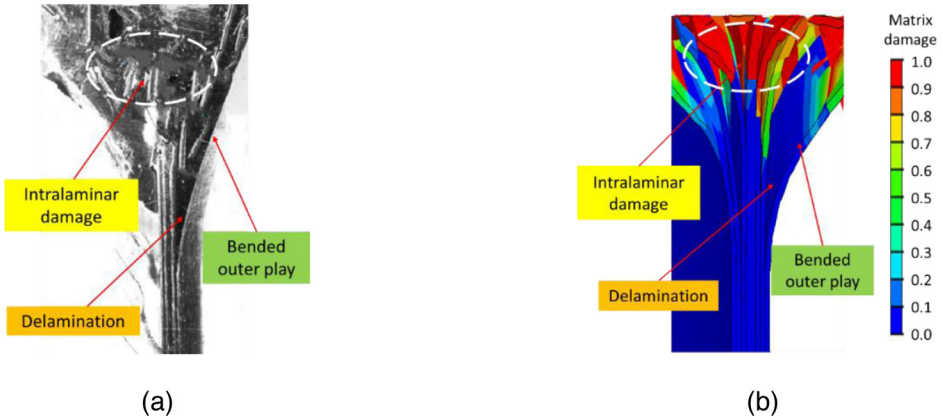

Fig. 9. Comparison of the side views of the crushed cylindrical tubes: (a) the experimentally observed damage morphology [22] and (b) the numerically predicted damage morphology.

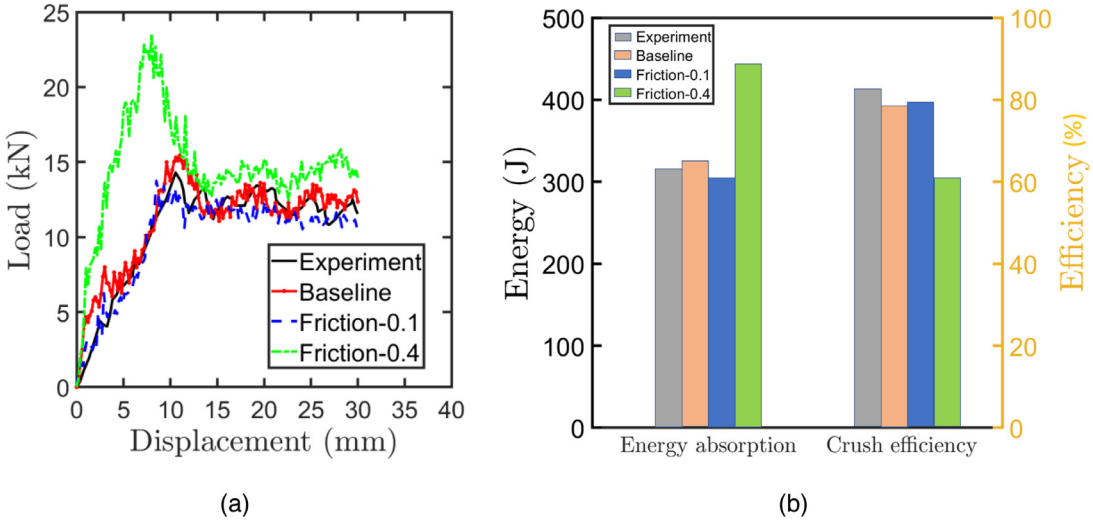

Fig. 10. Comparison between the results obtained from simulations with different friction coefficients: (a) load versus displacement curves, (b) energy absorption and crush efficiency.

Table 2
Interlaminar, intralaminar and total damage energy obtained from numerical simulations with different friction coefficients.

Cases with different friction coefficient	Interlaminar damage energy (J)	Intralaminar damage energy (J)	Total damage energy (J)
Baseline	129.8	202.9	332.7
Friction-0.1	130.7	167.4	298.1
Friction-0.4	149.4	293.1	442.5

presented by the models with the baseline coefficient value (79.6%) and the reduced coefficient value (80.9%). The results indicated that both the models with the baseline value and a value of 0.1 presented a good agreement with the experiment for both the energy absorption and crush efficiency. The details of interlaminar, intralaminar and total damage energy obtained from numerical simulations with different friction coefficients are presented in Table 2. It was observed that with the increasing friction coefficient, the total damage energy also shows a increasing trend, and the ratio of intralaminar damage energy also shows a positive relation with the increasing friction coefficient.

To further exhibit the effects of friction coefficient, damage morphologies obtained from models with different friction coefficients are compared in Figs. 11 and 12. These morphologies were captured when the crush displacement equals 10 mm. The highlights in Fig. 10 reflect the extent of fibre damage in the virtual cylindrical tubes. It can be found that the virtual tube with a coefficient of 0.4 presented the most fibre damage and the model with friction coefficient of 0.1 showed the least amidst these three simulation cases. This is deemed to be caused by the larger friction force between the compression plate and the composite tube, which constrained the movement of the material to peripheral area and increased the stress concentration in the contract region.

Fig. 12 shows the matrix damage in the virtual composite tube subjected to axial crush loading. The comparison between these three simulation cases with different friction coefficients indicated that the model with friction coefficient of 0.1 shows less matrix damage than other two cases. The extents of matrix damage presented by the model with values of 0.4 and baseline values are very close, but the case with 0.4 coefficient got more elements deleted. All these morphologies with fibre and matrix damage indicate that larger friction coefficient may lead to more damage and then more energy dissipation in the composite tube subjected to crush loading.

5.2. Effects of the blocking plies

To investigate the effects of blocking plies on the crushing performance of composite laminates, the baseline composite layup $[0/90]_{2S}$, the 0° blocking composite layup $[90/0_2/90]_S$ and the 90° blocking composite layup $[0/90_2/0]_S$ were employed in the crush simulation. The numerical results obtained from these three composite layups have been compared in Fig. 13, in which the experimental results were also presented for the sake of comparison. Fig. 13a shows the load versus displacement traces obtained from the simulations performed on different composite layups. The maximum loads shown by 0° blocking layup or the 90° blocking layup are 12.7 kN and 13.2 kN respectively, which are very close to each other. While more obvious difference was observed for the steady-state loads, which are 9.5 kN and 10.9 kN respectively. It can be found that either the 0° blocking layup or the 90° blocking layup presents lower maximum load and steady-state load compared to the baseline layup. The obtained energy absorption and crush efficiency were compared in Fig. 13b, for the investigated composite layups. It can be found that the composite layups with 0° or 90° blocking plies presented lower energy absorption values than the baseline composite layup (284.9 J for the 0° blocking layup and 253.7 J for the 90° blocking layup). In terms of crush efficiency, these results obtained from these studied three layups are very similar, in detail, the values of crush efficiency are 79.6% for baseline layup, 83.2% for 0° blocking layup and 77.6% for 90° blocking layup.

The fibre and matrix damage were also extracted from the simulations with different composite layups, to show the effects of ply blocking on the crush behaviour of composite tubes. Fig. 14 shows the fibre damage obtained from composite tubes with different layups, when crush displacement equals 10 mm. It can be found that both the composite tube with 0° ply blocking $[90/0_2/90]_S$ and the composite tube with 90° ply blocking $[0/90_2/0]_S$ tend to present less fibre damage than the composite tube with the baseline layup $[0/90]_{2S}$. Generally, composite layup with thick plies (blocked plies) tends to be delaminated easier compared with those with thin plies [46,47]. Delamination can decrease the stiffness of the laminated composites, which will then become less stiff. As a result, under the same loading condition, the composite tubes with blocked plies will present less fibre damage compared with the composite tube with baseline layup.

Correspondingly, the matrix damage from composite tubes with different layups have been obtained when crush displacement equals

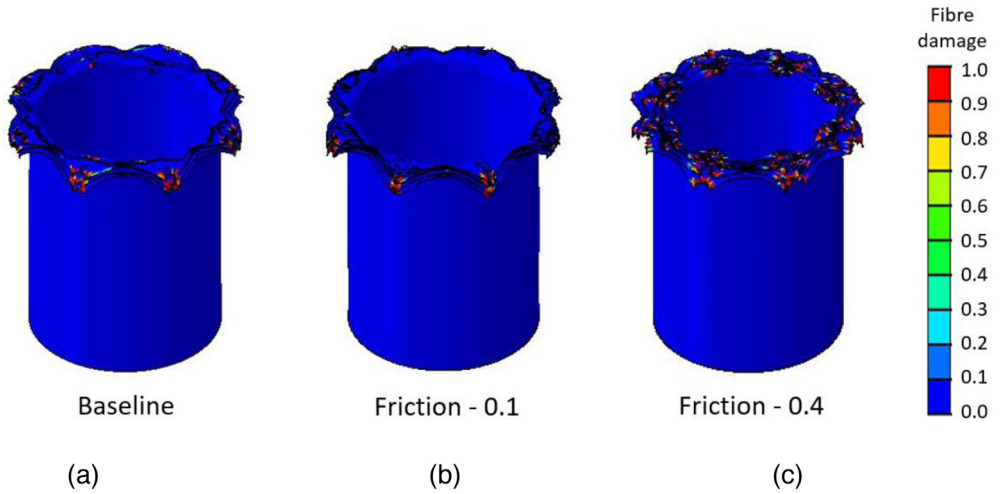

Fig. 11. Fibre damage presented by models with different friction coefficients: (a) the model with the baseline value, (b) the model with a value of 0.1 and (c) the model with a value of 0.4.

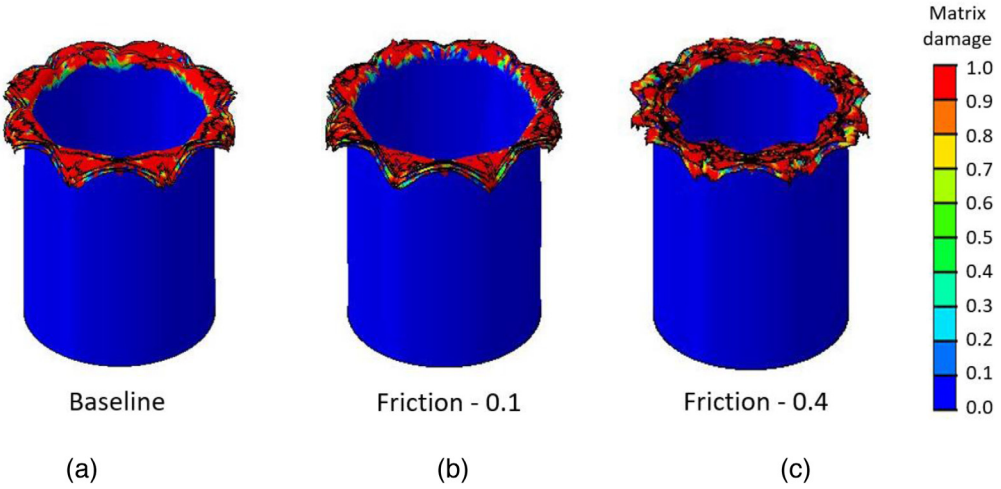

Fig. 12. Matrix damage presented by models with different friction coefficients: (a) the model with the baseline value, (b) the model with a value of 0.1 and (c) the model with a value of 0.4.

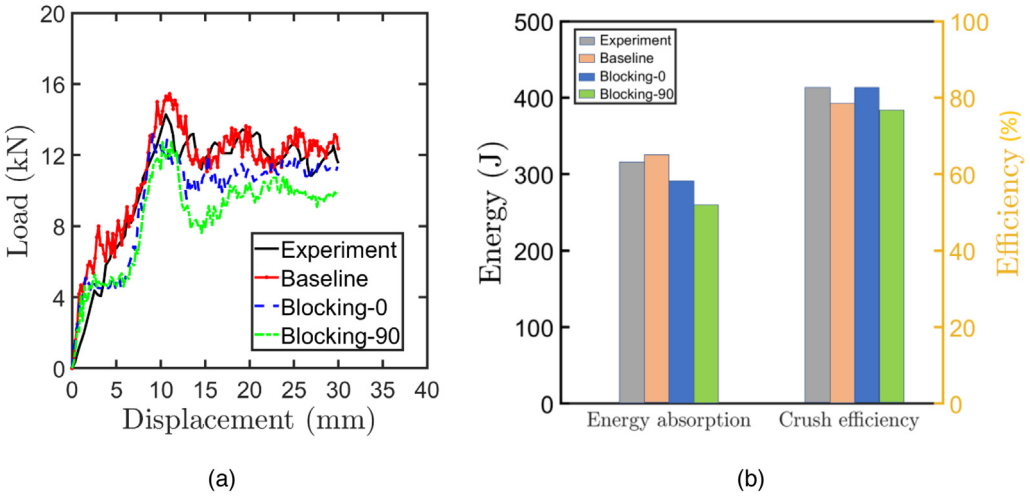

Fig. 13. Comparison between the results obtained from simulations with different layups: (a) load versus displacement curves, (b) specific energy absorption and crush efficiency.

10 mm and shown in Fig. 15. All these three composite layups exhibited considerable amount of matrix damage and element deletion due to the high stress and large deformation in the crush front region. It can be observed that the highlighted area (matrix damage) of tube with 90°

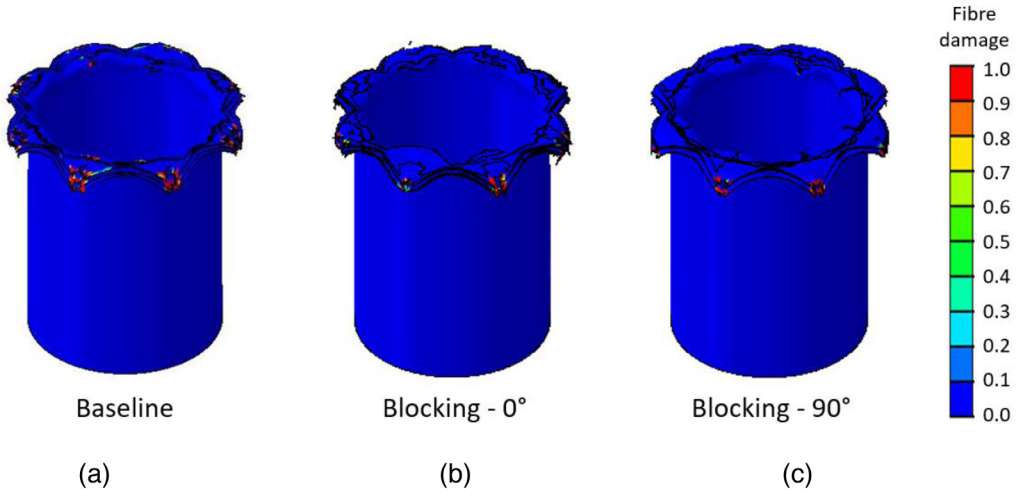

Fig. 14. Fibre damage presented by models with different layups: (a) the model with the baseline layup, (b) the model with blocking of 0° plies and (c) the model with blocking of 90° plies.

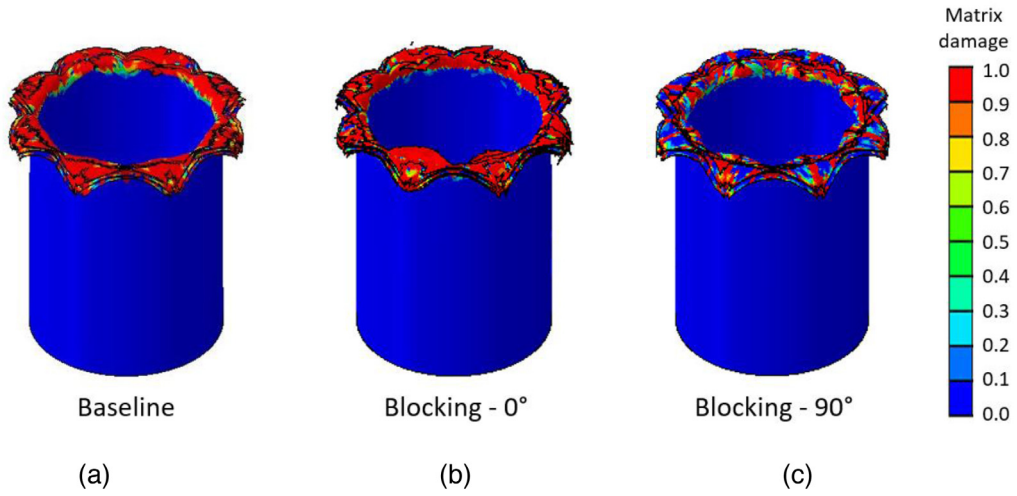

Fig. 15. Matrix damage presented by models with different layups: (a) the model with the baseline layup, (b) the model with blocking of 0° plies and (c) the model with blocking of 90° plies.

blocking plies were less than other two types of tubes. This is because when subjected to crush loading, outer 90° blocking plies tend to reach the limit of load-carrying capability first. As a result, the composite tubes, with 90° ply blocking, would get element deletion in the blocked plies first and tend to show less highlighted area in the figure, compared to the tubes with baseline layup and 0° ply blocking. Due to the deletion of elements in the blocking 90° plies, the remaining normal 0° plies lost the support from neighbouring plies, which will then reduce the loading carrying capability and energy absorption performance. The tube with 0° ply blocking showed very similar matrix damage extent with the tube with baseline layup, at the crush front region.

Through the observations from both the fibre damage and the matrix damage, it can be deduced that the composite tube with the baseline layup can efficiently involve all composite plies in the loading reaction and thus present a better residual load carrying capability, which then enable the baseline structures to absorb more energy during the crush event, through associated damage mechanisms, e.g., delamination, fibre and matrix damage.

6. Conclusions

This research presents a continuum damage mechanics based computational model, which can be used to evaluate the crushing performance of carbon–fibre reinforced composite structures. The experimental results, obtained from the crush experiments performed on the tulip-triggered cylindrical tube, were employed to validate the capability of the presented damage model in predicting the load response, energy absorption and damage morphology of composite structures. Excellent qualitative and quantitative correlation was achieved between experiment and simulation. The comparison between the experimental and modelling results have indicated that the high-fidelity three-dimensional elastic–plastic damage model was able to provide details of damage evolution in different composite structures, revealing a complex interaction between fibre fracture, matrix cracking and delamination. The validated computational model was then employed to study the effects of friction coefficient and blocking plies on the crushing performance of composite laminates. The simulation results

indicated that the higher friction coefficient led to more energy absorption but lower crush efficiency. Either the 0° or 90° blocking plies in the composite laminates tend to result in a worse crushing performance, due to the early element deletion in blocking plies and reduction in load carrying capability. The predictive capability of the computational model enabled the response of crush specimens with different features to be studied in detail with a focus on loading response and damage morphology, which can benefit the efficient design of composite structures.

CRediT authorship contribution statement

Haibao Liu: Writing – review & editing, Writing – original draft, Visualization, Validation, Methodology, Investigation, Formal analysis, Conceptualization. **Jin Zhou:** Writing – review & editing, Methodology, Investigation. **Di Zhang:** Writing – review & editing, Visualization, Investigation. **Shipeng Li:** Writing – review & editing, Methodology, Investigation. **Ioannis Giannopoulos:** Writing – review & editing.

Declaration of competing interest

The authors declare that they have no known competing financial interests or personal relationships that could have appeared to influence the work reported in this paper.

Data availability

Data will be made available on request.

Acknowledgement

Supports from the Research Computing Team at Cranfield University in accessing the high-performance computing facilities are gratefully acknowledged.

References

[1] C. Barile, C. Casavola, F. de Cillis, Mechanical comparison of new composite materials for aerospace applications, Composites B 162 (2019) 122–128, http://dx.doi.org/10.1016/j.compositesb.2018.10.101.

[2] R. Degenhardt, S.G.P. Castro, M.A. Arbelo, R. Zimmerman, R. Khakimova, A. Kling, Future structural stability design for composite space and airframe structures, Thin-Walled Struct. 81 (2014) 29–38, http://dx.doi.org/10.1016/j.tws.2014.02.020.

[3] P. Mårtensson, D. Zenkert, M. Åkermo, Cost and weight efficient partitioning of composite automotive structures, Polym. Compos. 38 (2017) 2174–2181, http://dx.doi.org/10.1002/pc.23795.

[4] J. Striewe, C. Reuter, K.H. Sauerland, T. Tröster, Manufacturing and crashworthiness of fabric-reinforced thermoplastic composites, Thin-Walled Struct. 123 (2018) 501–508, http://dx.doi.org/10.1016/j.tws.2017.11.011.

[5] LS-DYNA, Keyword User's Manual Volume I, Livermore Software Technology Corporation (LSTC), 2013.

[6] Engineering Systems International, PAM-CRASH 2G. F-94578 Rungis Cedex, France, 2009.

[7] Abaqus 2018 Documentation, Dassault Systèmes, Providence, Rhode Island, USA, 2018.

[8] Z. Wang, X. Jin, Q. Li, G. Sun, On crashworthiness design of hybrid metal-composite structures, Int. J. Mech. Sci. 171 (2020) 105380, http://dx.doi.org/10.1016/j.ijmecsci.2019.105380.

[9] H. Jiang, Y. Ren, B. Gao, Research on the progressive damage model and trigger geometry of composite waved beam to improve crashworthiness, Thin-Walled Struct. 119 (2017) 531–543, http://dx.doi.org/10.1016/j.tws.2017.07.004.

[10] M. Anghileri, E.C. Chirwa, L. Lanzi, F. Mentuccia, An inverse approach to identify the constitutive model parameters for crashworthiness modelling of composite structures, Compos. Struct. 68 (2005) 65–74, http://dx.doi.org/10.1016/j.compstruct.2004.03.001.

[11] X. Xiao, M.E. Botkin, N.L. Johnson, Axial crush simulation of braided carbon tubes using MAT58 in LS-DYNA, Thin-Walled Struct. 47 (2009) 740–749, http://dx.doi.org/10.1016/j.tws.2008.12.004.

[12] A.F. Johnson, M. David, Failure mechanisms in energy-absorbing composite structures, Phil. Mag. 90 (2010) 4245–4261, http://dx.doi.org/10.1080/14786435.2010.497471.

[13] D. Dalli, L.F. Varandas, G. Catalanotti, S. Foster, B.G. Falzon, Assessing the current modelling approach for predicting the crashworthiness of formula one composite structures, Composites B (2020) 108242, http://dx.doi.org/10.1016/j.compositesb.2020.108242.

[14] W. Tan, B.G. Falzon, M. Price, H. Liu, The role of material characterisation in the crush modelling of thermoplastic composite structures, Compos. Struct. 153 (2016) 914–927, http://dx.doi.org/10.1016/j.compstruct.2016.07.011.

[15] H. Liu, B.G. Falzon, J.P. Dear, An experimental and numerical study on the crush behaviour of hybrid unidirectional/woven carbon-fibre reinforced composite laminates, Int. J. Mech. Sci. 164 (2019) http://dx.doi.org/10.1016/j.ijmecsci.2019.105160.

[16] H.A. Israr, S. Rivallant, C. Bouvet, J.J. Barrau, Finite element simulation of 0/90 CFRP laminated plates subjected to crushing using a free-face-crushing concept, Composites A 62 (2014) 16–25, http://dx.doi.org/10.1016/j.compositesa.2014.03.014.

[17] W. Tan, B.G. Falzon, Modelling the crush behaviour of thermoplastic composites, Compos. Sci. Technol. 134 (2016) 57–71, http://dx.doi.org/10.1016/j.compscitech.2016.07.015.

[18] W. Tan, B.G. Falzon, Modelling the nonlinear behaviour and fracture process of AS4/PEKK thermoplastic composite under shear loading, Compos. Sci. Technol. 126 (2016) 60–77, http://dx.doi.org/10.1016/j.compscitech.2016.02.008.

[19] H. Liu, J. Liu, Y. Ding, Z.E. Hall, X. Kong, J. Zhou, R.K. Bamber, A three-dimensional elastic–plastic damage model for predicting the impact behaviour of fibre-reinforced polymer–matrix composites, Composites B 201 (2020) 1–30, http://dx.doi.org/10.1016/j.compositesb.2020.108389.

[20] H. Liu, B.G. Falzon, S. Li, W. Tan, J. Liu, H. Chai, B.R.K. Blackman, J.P. Dear, Compressive failure of woven fabric reinforced thermoplastic composites with an open-hole: an experimental and numerical study, Compos. Struct. 213 (2019) 108–117, http://dx.doi.org/10.1016/J.COMPSTRUCT.2019.01.070.

[21] H. Liu, J. Liu, Y. Ding, J. Zhou, X. Kong, L.T. Harper, B.R.K. Blackman, B.G. Falzon, J.P. Dear, Modelling damage in fibre-reinforced thermoplastic composite laminates subjected to three-point bend loading, Compos. Struct. 236 (2020) 111889, http://dx.doi.org/10.1016/j.compstruct.2020.111889.

[22] L.N.S. Chiu, B.G. Falzon, D. Ruan, S. Xu, R.S. Thomson, B. Chen, W. Yan, Crush responses of composite cylinder under quasi-static and dynamic loading, Compos. Struct. 131 (2015) 90–98, http://dx.doi.org/10.1016/j.compstruct.2015.04.057.

[23] A. Puck, H. Schürmann, Failure analysis of FRP laminates by means of physically based phenomenological models, Compos. Sci. Technol. 58 (1998) 1045–1067, http://dx.doi.org/10.1016/S0266-3538(01)00208-1.

[24] G. Catalanotti, P.P.P. Camanho, A.T.T. Marques, Three-dimensional failure criteria for fiber-reinforced laminates, Compos. Struct. 95 (2013) 63–79, http://dx.doi.org/10.1016/j.compstruct.2012.07.016.

[25] A. Puck, H. Schürmann, Failure analysis of FRP laminates by means of physically based phenomenological models, Compos. Sci. Technol. 58 (1998) 1045–1067, http://dx.doi.org/10.1016/S0266-3538(01)00208-1.

[26] ASTM, Standard Test Method for Mixed Mode I-Mode II Interlaminar Fracture Toughness of Unidirectional Fiber Reinforced Polymer Matrix Composites, D6671/D 6671M-14, West Conshohocken, PA, 2014, http://dx.doi.org/10.1520/E0384-10.

[27] C.T. Sun, J.L. Chen, A simple flow rule for characterizing nonlinear behavior of fiber composites, J. Compos. Mater. 23 (1989) 1009–1020, http://dx.doi.org/10.1177/002199838902301004.

[28] J.K. Chen, F.A. Allahdadi, C.T. Sun, A quadratic yield function for fiber-reinforced composites, J. Compos. Mater. 31 (1997) 788–811.

[29] C.T. Sun, Y. Rui, Orthotropic elasto-plastic behavior of AS4/PEEK thermoplastic composite in compression, Mech. Mater. 10 (1990) 117–125, http://dx.doi.org/10.1016/0167-6636(90)90022-8.

[30] K.J. Yoon, C.T. Sun, Characterization of elastic-viscoplastic properties of an AS4/PEEK thermoplastic composite, J. Compos. Mater. 25 (1991) 1277–1296, http://dx.doi.org/10.1177/002199839102501002.

[31] T. Yokozeki, S. Ogihara, S. Yoshida, T. Ogasawara, Simple constitutive model for nonlinear response of fiber-reinforced composites with loading-directional dependence, Compos. Sci. Technol. 67 (2007) 111–118, http://dx.doi.org/10.1016/j.compscitech.2006.03.024.

[32] M.V. Donadon, L. Iannucci, B.G.G. Falzon, J.M. Hodgkinson, S.F.M. De Almeida, A progressive failure model for composite laminates subjected to low velocity impact damage, Comput. Struct. 86 (2008) 1232–1252, http://dx.doi.org/10.1016/j.compstruc.2007.11.004.

[33] W. Tan, B.G. Falzon, Modelling the crush behaviour of thermoplastic composites, Compos. Sci. Technol. 134 (2016) 57–71, http://dx.doi.org/10.1016/j.compscitech.2016.07.015.

[34] B.G. Falzon, P. Apruzzese, Numerical analysis of intralaminar failure mechanisms in composite structures. Part II: Applications, Compos. Struct. 93 (2011) 1047–1053, http://dx.doi.org/10.1016/j.compstruct.2010.06.028.

[35] A. Faggiani, B.G. Falzon, Predicting low-velocity impact damage on a stiffened composite panel, Composites A 41 (2010) 737–749, http://dx.doi.org/10.1016/j.compositesa.2010.02.005.

[36] B.G. Falzon, H. Liu, W. Tan, Comment on a tensorial based progressive damage model for fiber reinforced polymers, Compos. Struct. 176 (2017) 877–882, http://dx.doi.org/10.1016/j.compstruct.2017.06.011.

[37] H. Liu, B.G. Falzon, W. Tan, Experimental and numerical studies on the impact response of damage-tolerant hybrid unidirectional/woven carbon-fibre reinforced composite laminates, Composites B 136 (2018) 101–118, http://dx.doi.org/10.1016/j.compositesb.2017.10.016.

[38] P. Feraboli, B. Wade, F. Deleo, M. Rassaian, M. Higgins, A. Byar, LS-DYNA MAT54 modeling of the axial crushing of a composite tape sinusoidal specimen, Composites A 42 (2011) 1809–1825, http://dx.doi.org/10.1016/j.compositesa.2011.08.004.

[39] A. Cherniaev, C. Butcher, J. Montesano, Predicting the axial crush response of CFRP tubes using three damage-based constitutive models, Thin-Walled Struct. 129 (2018) 349–364, http://dx.doi.org/10.1016/j.tws.2018.05.003.

[40] P. Feraboli, Development of a corrugated test specimen for composite materials energy absorption, J. Compos. Mater. 42 (2008) 229–256, http://dx.doi.org/10.1177/0021998307086202.

[41] L.N.S. Chiu, B.G. Falzon, B. Chen, W. Yan, Validation of a 3D damage model for predicting the response of composite structures under crushing loads, Compos. Struct. 147 (2016) 65–73, http://dx.doi.org/10.1016/j.compstruct.2016.03.028.

[42] W. Tan, B.G. Falzon, M. Price, Predicting the crushing behaviour of composite material using high-fidelity finite element modelling, Int. J. Crashworthiness 20 (2015) 60–77, http://dx.doi.org/10.1080/13588265.2014.972122.

[43] L.N.S. Chiu, B.G. Falzon, R. Boman, B. Chen, W. Yan, Finite element modelling of composite structures under crushing load, Compos. Struct. 131 (2015) 215–228, http://dx.doi.org/10.1016/j.compstruct.2015.05.008.

[44] A. Riccio, A. De Luca, G. Di Felice, F. Caputo, Modelling the simulation of impact induced damage onset and evolution in composites, Composites B 66 (2014) 340–347, http://dx.doi.org/10.1016/j.compositesb.2014.05.024.

[45] W. Tan, B.G. Falzon, M. Price, H. Liu, The role of material characterisation in the crush modelling of thermoplastic composite structures, Compos. Struct. 153 (2016) 914–927, http://dx.doi.org/10.1016/j.compstruct.2016.07.011.

[46] S. Sihn, R.Y. Kim, K. Kawabe, S.W. Tsai, Experimental studies of thin-ply laminated composites, Compos. Sci. Technol. 67 (2007) 996–1008, http://dx.doi.org/10.1016/j.compscitech.2006.06.008.

[47] J. Galos, Thin-ply composite laminates: a review, Compos. Struct. 236 (2020) 111920, http://dx.doi.org/10.1016/j.compstruct.2020.111920.